

# Molecular dynamics simulation of fluid containing gas in hydrophilic rough wall nanochannels

Tsu-Hsu Yen

Received: 20 June 2013 / Accepted: 19 November 2013 / Published online: 30 November 2013  
© Springer-Verlag Berlin Heidelberg 2013

**Abstract** This study performed the molecular dynamic simulations to investigate the boundary behavior of liquid water with entrapped gas bubbles over various hydrophilic roughened substrates. A “liquid–gas–vapor coexistence setup” was employed to maintain a constant thermodynamic state during individual equilibrium simulations and corresponding non-equilibrium Poiseuille flow cases. The two roughened substrates (Si(100) and graphite) adopted in this study present similar contact angles and slip length with gas-free fluid. By considering the effects of argon molecules at the interface, we demonstrated that the boundary slip behavior differed dramatically between these two rough wall channels. This divergence can be attributed to differences in the morphology of argon bubble at the interface due to discrepancies in the atomic arrangement and wall–fluid interaction energy. Furthermore, the density of gas at the interface had a significant impact on the effective slip length of the roughened graphite substrate, whereas shear rate  $\dot{\gamma}$  presented no noticeable influence. On the roughened Si(100) surface, the morphology of the argon bubbles exhibited far higher meniscus curvature and unstable properties under hydrodynamic effects. Thus, this substrate exhibited no slip to slight negative slip and no remarkable influence from either the density of gas at the interface or shear rate. In the present study, we demonstrate that the morphology and behavior of interfacial gas bubbles are influenced by the parameters of wall–fluid interaction as well as the atomic arrangement of the substrate. Our results related to nanochannel flow reveal that different

surfaces, such as Si(100) and graphite, may possess similar intrinsic wettability; however, properties of the interfacial gas bubbles can lead to noticeable changes in interfacial characteristics resulting in various degrees of boundary slippage.

**Keywords** Apparent slip length · Fluid containing gas · Interfacial properties · Molecular dynamic

## 1 Introduction

Various phenomena of solid–fluid interfaces have been attracting considerable attention due to their importance in many areas of engineering and applied sciences. Surface effects are more pronounced in micro- and nanochannels than in macroscopic systems due to the high surface-to-volume ratio. Interfacial phenomena, such as wettability and boundary slippage, are important issues in nanofluidics. Differences between the flow characteristics at the nanoscale and macroscale can be attributed to interactions at the atomic level. A number of key reviews of microscopic wall–fluid interfacial investigations have been conducted. Bocquet and Barrat (2007) investigated heat transport and slip at various scales, while Cao et al. (2009) discussed interfacial phenomena from the point of view of molecular momentum transport. However, the underlying mechanisms of interfacial phenomena have yet to be elucidated (Lauga et al. 2005).

Researchers have recently demonstrated the existence of apparent slip in liquid flowing across a solid surface (Vinogradova and Belyaev 2011; Maali et al. 2008; Tretheway and Meinhart 2004). Various experimental results indicate that the observed slip is not artificial, which opens the door to debate concerning the wide range of slip lengths that

---

T.-H. Yen (✉)  
Department of Electrical Engineering, Chinese Naval Academy,  
No. 669 Chun Hsiao Rd., Tsoying, Kaohsiung 813,  
Taiwan, ROC  
e-mail: g960403@gmail.com

have been observed, from a few nanometers (Maali et al. 2008) to several micrometers (Tretheway and Meinhart 2004). Other researchers have drawn a contradictory conclusion that roughness either induces large slip (Bonaccorso et al. 2003) or decreases slippage (Zhu and Granick 2002), even on roughened hydrophilic surfaces. These debates stem from an insufficient understanding of the complex properties of boundary slip, which involves the interplay of numerous physical and chemical factors (Harting et al. 2010). The higher slip lengths observed in experiments tend to occur on smooth hydrophobic surfaces (Zhu and Granick 2001) or topologically patterned substrates (Quééré 2008).

Argyris et al. (2008) investigated the structural and dynamic properties of water molecules proximal to graphite and silica surfaces and found that the hydrogen bond of water on interfacial area was influenced by solid surface hydroxyl density, which altered the interfacial properties. Sendner et al. (2009) indicated that wall–fluid slippage depends on the existence of a depletion layer in which the fluid adopts a substantially lower viscosity, which can be considered a vapor state. In addition, the existence and influence of solid–fluid interfacial layering structures have also been proven in many previous MD simulations (e.g. Soong et al. 2007; Sofos et al. 2012, 2013). These results indicate that the interfacial structure is influenced by a range of factors (Sofos et al. 2013) including the lattice orientation (Soong et al. 2007) and solid structure (Ho et al. 2011), nanochannel size (Sofos et al. 2009), surface charge (Joly et al. 2004), surface morphology (Cao et al. 2006), fluid shear rate (Thompson and Troian 1997), hydrogen bonding (Joseph and Aluru 2008; Argyris et al. 2008), pressure (Cottin-Bizonne et al. 2003; Tretyakov and Müller 2013), temperature (Sofos et al. 2013), and dissolved gasses (Dammer and Lohse 2006; Sendner et al. 2009). Moreover, the liquid may slide on the gas film; therefore, the nanobubbles comprise gas rather than vapor and are often observed coexisting with the depletion region (Tandon and Kirby 2008), playing the important role of larger slip (Hyväluoma et al. 2011).

The influence of surface roughness and gas molecules is particularly pronounced. A roughened surface can be fabricated with surface elements rising from or grooves indented into the solid surface of the substrate. A number of previous MD simulations have dealt with the effects of surface obstacles or grooves on nanoscale flow and electro-osmotic flow (Kim and Darve 2006). Priezjev et al. (2005) investigated the anisotropic flow across planar-stripped substrates under mixed boundary conditions. Gordillo and Martí (2010) studied the influence of surface roughness on the static and dynamic properties of water on graphene. Their results indicate that the amplitude of the surface features, rather than particular type (random or periodic),

determine water adsorption properties. More recently, Tretyakov and Müller (2013) investigated polymer flow passing across a rough substrate: their results demonstrate a gradual crossover between Wenzel state and the Cassie state within surface cavities. Using dissipative particle dynamics (DPD) simulation, Kasiteropoulou et al. (2012) investigated the flow through periodically grooved nanochannels as well as the behavior of fluid particles trapped within the cavities. Using a lattice Boltzmann method (LBM), Sbragaglia et al. (2006) studied surface roughness hydrophobicity coupling in nanochannels with grooved surfaces.

Micro- or nano-textured surfaces with grooves or cavities may produce micro- or nano-sized bubbles or a gaseous layer. In these cases, low viscosity gas bubbles act as a lubricant, resulting in large apparent slip. Gao and Feng (2009) performed numerical simulations of shear flow over a patterned substrate with entrapped gas bubbles. They determined that the apparent slip length depends on the morphology of the menisci and hence on the shear rate. Using LBM, Hyväluoma and Harting (2008) determined that air bubbles can result in negative slip and that slip length decreased with an increase in shear rate. However, they overlooked the depinning and slippery effects of gas bubbles. Due to high surface tension in the surrounding water at the nanoscale, gaseous structures are condensed to higher densities, which can alter the behavior of the gases. The physical mechanisms associated with the nanobubbles contained within fluids in nanochannels may differ from the macro-scale and therefore requires further investigation.

The above brief review of previous relevant literature reveals a number of interesting issues worthy of further investigation. Water is the most common liquid in nature and the most important fluid in scientific and engineering applications. Argon can be used to represent the case of gas in a liquid. Silicon and graphite are very important materials in micro/nano-fabrication. This study applied water containing argon molecules to silicon and graphite nanochannels with roughened walls as a model to investigate the influence of hydrophilic solid materials on boundary conditions. We also examined the effects of interfacial argon density and shear rate. Finally, we analyzed general fluidic properties in cases of hydrostatic and hydrodynamic states including effective slip length, density, and average hydrogen bond distributions as well as gas bubble menisci. Simulations were first performed using gas-free water before examining the effects of argon density and shear rate at the interface between the liquids and two different textured materials.

## 2 Methodology and simulation model

This study modeled hydrostatic wetting and Poiseuille flow phenomena on Si(100) and graphite substrates using MD

**Fig. 1** Atomic arrangement of (a) silicon, in which the two colors denote the two face centered cubic (fcc) structures and (b) graphite, in which adjacent atomic layers are represented by different colors (color figure online)

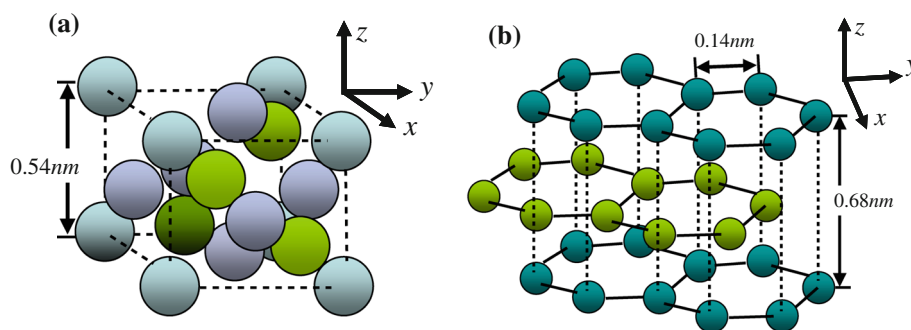


**Table 1** Charges and Lennard-Jones parameters adopted for the current simulations

Ion/molecule	$q_i(e)$	$\sigma_{\alpha\beta}/\sigma, \sigma = \sigma_{oo}$	$\epsilon_{\alpha\beta}/\epsilon, \epsilon \equiv \epsilon_{oo}$
O ↔ O (H <sub>2</sub> O)	-1.04	$\sigma_{oo} = 0.3154 \text{ nm}$	$\epsilon_{oo} = 0.155 \text{ kcal}$
H ↔ H (H <sub>2</sub> O)	0.52	0	0
Si ↔ H <sub>2</sub> O		$\sigma_{Si-O}/\sigma = 1.0315$	$\epsilon_{Si-O}/\epsilon = 2.0$
C ↔ H <sub>2</sub> O		$\sigma_{C-O}/\sigma = 1.012$	$\epsilon_{C-O}/\epsilon = 0.667$
Ar ↔ Ar		$\sigma_{Ar-Ar}/\sigma = 1.0812$	$\epsilon_{Ar-Ar}/\epsilon = 1.538$
Ar ↔ H <sub>2</sub> O		$\sigma_{Ar-O}/\sigma = 1.045$	$\epsilon_{Ar-O}/\epsilon = 1.242$
Si ↔ Ar		$\sigma_{Si-Ar}/\sigma = 1.132$	$\epsilon_{Si-Ar}/\epsilon = 0.81$
C ↔ Ar		$\sigma_{C-Ar}/\sigma = 1.108$	$\epsilon_{C-Ar}/\epsilon = 0.81$

simulations. These surfaces were selected because they have different atomic arrangements (shown in Fig. 1) and wall–fluid interaction parameters (shown in Table 1) but similar intrinsic contact angles (Yen 2011). At the microscopic scale, a Si(100) surface presents higher atomic roughness and solid–fluid interaction energy than does a graphite surface. The substrates in this study were produced by deleting specific solid atoms to form periodic grooves (Fig. 1). In the atomic structure of the graphite (0001) substrate, the normal plane (the plane parallel to z axis) has a relatively loose arrangement and the tangential plane (x–y plane) has a tighter arrangement. In contrast, the Si(100) substrate presents similar arrangements for both the normal and tangential planes. Microscopic parameters, including wall–fluid interaction energy, length, and atomic arrangement, alter the fluid dynamics near the rough surfaces. Two particular properties of the graphite substrate are higher epitaxial layering distribution in the adjacent fluid and relatively high hydrophobic grooves induced by its unique atomic arrangement and low water–graphite interfacial energy.

This study employed the “liquid–gas–vapor coexistence” procedure, similar to the method outlined by Cao et al. (2006), in which a constant thermodynamic state is maintained for individual simulation cases. The simulation followed the procedures presented in Fig. 2. As an initial condition, a sandwich-like cube containing water

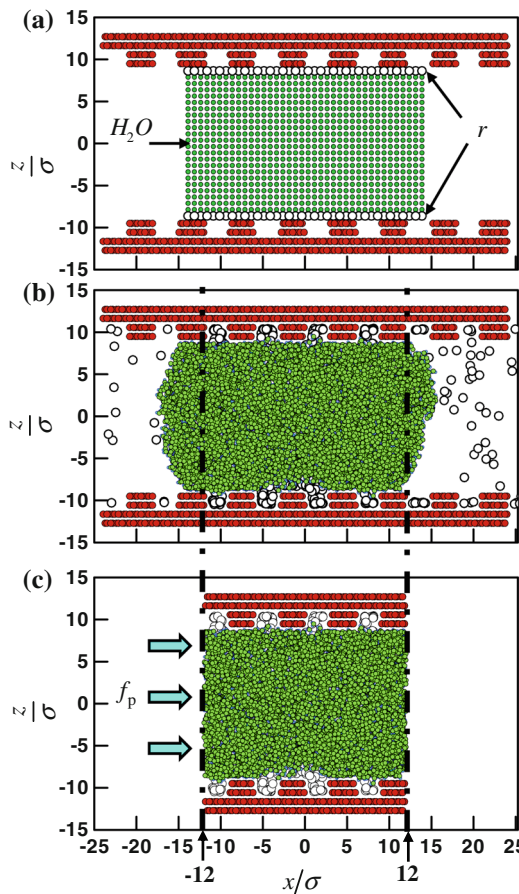


**Fig. 2** Simulation system and its three-stage assembly: a initial setup stage, b hydrostatic simulation stage: argon–water–vapor coexisting in the nanochannels, and c hydrodynamic simulation stage: Poiseuille flow in the nanochannels

molecules was confined between two layers of argon molecules within a channel in the substrate.

The number of argon particles was varied to simulate various cases of interfacial argon density. The simulations were then initiated with the system driven until it reached a steady thermodynamic state, thereby approaching a state of coexistence between the water and argon. This enabled the sampling of the properties of equilibrium, such as the number of hydrogen bonds and fluid density. Following the

completion of the equilibrium simulation, the middle section was segmented along the  $x$  direction to form a flow configuration. The Poiseuille flow system under consideration comprised water and argon molecules confined between two parallel substrates under the same thermodynamic conditions as those used in the hydrostatic equilibrium simulation cases. In the current non-equilibrium Poiseuille flow simulation, a constant external force stemming from the pressure gradient in the  $x$  direction was applied to the particles within the fluid. Due to the high thermal noise of fluid particle, strong external force fields ( $f_p = 0.01 - 0.05\sigma^3/\varepsilon$  corresponding to  $1 \times 10^{12} - 5 \times 10^{12} \text{ m/s}^2$ ) are necessary to determine the fluid velocity with reasonable accuracy. The setting of force fields is similar to those of previous simulations (Joseph and Aluru 2008).

Data sampling was performed at a period of  $300 \tau$  to  $1,100 \tau$ , which corresponds to  $0.5\text{--}1.83 \text{ ns}$  ( $6 \times 10^5 - 2.2 \times 10^6$  time steps). In the current argon–water coexistence simulations, the systems contained approximately 7,000–8,500 water molecules. In the Poiseuille flow simulation, the systems contained approximately 4,000–5,500 water molecules. The dimensions of the fluid computational domain were  $L_x \times L_y \times L_z$ . The two computational domains were divided into a number of bins:  $\Delta x \times \Delta y \times \Delta z = 0.2\sigma \times L_y \times 0.2\sigma$  for two-dimensional contours and  $\Delta x \times \Delta y \times \Delta z = L_x \times L_y \times 0.2\sigma$  for one-dimensional profiles. In the case of the Poiseuille flow of a Newtonian fluid under constant external force, the macroscopic hydrodynamics provides a parabolic profile. This study sampled the averages of the velocity profiles for the fluid channel and grooves. This enables calculation of effective slip length by extrapolating the velocity profiles from the position in the fluid to the point at which the velocity would vanish. Slip length  $L_s$ , as a measure of fluid slippage, was defined in the Navier slip formula  $L_s = u_s / (du_x/dz)_W$  where  $u_s$  stands for the slip velocity and  $(du_x/dz)_W$  for the fluid velocity gradient in the normal direction at the wall–fluid baseline. Slip length was obtained according to the second-order polynomial fit of the velocity; however, to avoid non-Newtonian effects, we excluded data related to the near-substrate regions that contain argon bubbles. In the current study, the baseline was defined as the position of  $0.5 \sigma$  above the upper-most level of solid atoms. The position of the baseline was determined according to the conclusion presented by Zhu et al. (2005), in which the authors proposed shifting the boundary conditions from the position of upper-most level of solid atoms to the edge of the zero-density region.

Figure 3 defines the period ( $\lambda$ ) and amplitude ( $A_p$ ) of the groove. In static simulations, the dimensions of the fluid computational domain were  $L_x \times L_y \times L_z = 48\sigma \times 12\sigma \times 19\sigma$  in the  $x$ ,  $y$ , and  $z$  directions. In the hydrodynamic

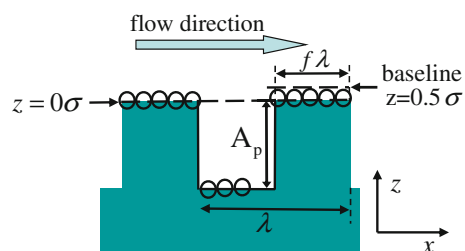


**Fig. 3** Schematic illustration of substrate with grooved patterns, where  $A_p$  denotes the height of the groove,  $\lambda$  the period of the pattern and  $f\lambda$  the spacing between two grooves in which  $f$  is the surface fraction

simulations, the dimensions of the fluid computational domain were  $L_x \times L_y \times L_z = 24\sigma \times 12\sigma \times 19\sigma$  in the  $x$ ,  $y$ , and  $z$  directions with  $L_z$  denoting the distance between the two upper-most levels of the substrate. Channel size alters the fluid transport properties, as demonstrated in a previous study (Sofos et al. 2009): this study investigated the flow of fluid through roughened nanochannels and discovered that the most noticeable variations occurred when the width of the channel was below  $15 \sigma$ . In addition, Argyris et al. (2008) reported that the dynamic behavior calculated at  $4.5 \sigma$  from the surface is isotropic. To avoid the interactive influence between the upper and lower interfaces, the dimensions of  $L_z$  were set to  $19 \sigma$ , a similar limit to that used in previous studies (Sofos et al. 2009, 2012; Sendner et al. 2009). To determine the  $L_x$  dimension of static simulation, we considered the following. On the one hand, the second stage of simulation (shown in Fig. 2b) must reach a state of hydrostatic equilibrium with no vapor–liquid interface within the division segment (shown as the region between dash lines in Fig. 2b) for all calculations. On the other hand, a longer  $L_x$  would increase calculation complexity. In our simulation, the parameters of  $L_x$  and fluid particle number were set to  $48\sigma$  and 7,000–8,500, respectively. This provided satisfactory results for static distribution in a state of equilibrium.

In the current study, the parameters of the periodically patterned substrate were established as follows: amplitude  $A_p = 2.58\sigma$ , surface fraction  $f = 0.5$ , and period  $\lambda = 6\sigma$ . Martini et al. (2008) indicated that the results have no obvious difference between adopting the rigid wall model and flexible wall model when the shear rate were below  $\sim 0.08 \tau^{-1}$ . Since the shear rates in the present study are lower than the critical value, the wall atoms were treated as stationary to reduce calculation time.

The simulation model comprised water, argon molecules, and solid atoms. The solid boundary lies on the  $xy$ -plane, where periodic boundary conditions are posed in both the  $x$ - and  $y$ -directions. The TIP4P model (Rapaport 2004) was employed for the simulation of water molecules. A cutoff distance of  $r_c = 4.2\sigma$  was adopted for the Lennard-Jones



(LJ) and Coulomb interaction. The cutoff distance was applied in reference to the oxygen sites. The LJ and Coulomb interaction potentials employed in the current simulations were both truncated and shifted. The 12-6 LJ potential was used to measure the interaction between two oxygen atoms and between oxygen and solid atoms. Coulomb potential was applied to evaluate the interaction between charges. Parameter  $r$  indicates the separation distance between interacting molecules/atoms,  $\epsilon$  is an energy scale characterizing the strength of the interaction, and  $\sigma$  denotes a molecular length scale. Conventionally,  $\sigma$  is used for length,  $\epsilon$  for energy,  $\tau = (m\sigma^2/\epsilon)^{1/2}$  for time, and  $\epsilon/k_B T$  for temperature as reduced units in MD simulations. For water,  $e = 4.803 \times 10^{-10}$  esu,  $\sigma \equiv \sigma_{OO} = 3.154 \text{ \AA}$ ,  $\epsilon = 0.155$  kcal and  $\tau = 1.66 \times 10^{-12}$  s. Hereafter, the physical properties are presented in accordance with the reduced units mentioned above. The charges and Lennard-Jones parameters are adopted from the references (Sendner et al. 2009) and are summarized in Table 1.

Newton's equations of particle motion were solved using the predictor–corrector algorithm with the following time step:  $5 \times 10^{-4} \tau$ . In both hydrostatic and hydrodynamic simulation, the temperature within the system was set at 150 K, which remained unchanged until 5,000 time steps had elapsed. The temperature was then increased to 300 K at the 10,000th time step where it remained until the conclusion of the simulations.

The temperatures of water and argon molecules were controlled individually using the Nosé Hoover thermostat in both hydrostatic and hydrodynamic calculations. To minimize the influence on fluid flow, the thermostat was adopted only in the  $y$  direction, which is perpendicular to the direction of flow. The relaxation time, which controls the rate of heat transfer between the system and the reservoir, was set to 100 time steps to ensure satisfactory temperature control without introducing non-physical high-frequency temperature oscillations.

There are three criteria for determining whether a hydrogen bond is formed between two water molecules (Martí 1999): (a) The distance  $R_{OO}$  between the oxygen atoms of two molecules is smaller than  $R_{OO}^c$ ; (b) The distance  $R_{OH}$  between the hydrogen atom of the donor molecule and the oxygen atom of the acceptor is less than  $R_{OH}^c$ ; (c) The bond angle  $\phi$  between the O–O direction and the molecular O–H direction of the donor must be less than a critical value  $\phi^c$ , where H is the hydrogen that forms the bonds. The critical parameter values are  $R_{OO}^c = 3.6 \text{ \AA}$ ,  $R_{OH}^c = 2.4 \text{ \AA}$  and  $\phi^c = 30^\circ$ .

### 3 Results and discussion

Although differences in wettability and boundary slippage were expected due to differences in the solid–fluid

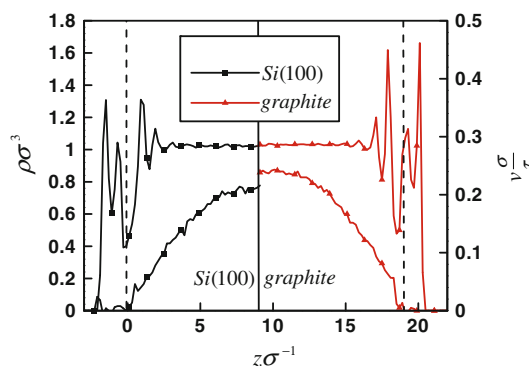


**Fig. 4** MD results of water density and velocity profiles within nanochannels of Si(100) (left plot) and graphite substrate (right plot). The dashed lines denote the position of the first layer of solid atoms

parameters and solid atomic arrangement, the contact angle and slip length of gas-free water were similar for roughened Si(100) and graphite substrates. The equilibrium simulations demonstrate that the contact angles of the roughened wall were  $87^\circ$  for the Si(100) and  $88^\circ$  for the graphite substrate. The results of Poiseuille flow revealed slip lengths of  $\sim 0.3\sigma$  for Si(100) and  $\sim 0.65\sigma$  for the graphite substrate. In the current study, the value for the contact angle is the mean value of angles between the base lines of the two substrates and the tangent of the vapor–fluid interfacial profiles. The base line is defined as the position of  $0.5\sigma$  above the innermost wall atoms and the curve profile is fitted according to specific density contours. An inspection of the density contours indicated that the contour shapes and contact angles did not change significantly within a water density range of  $0.35\text{--}0.85 \sigma^{-3}$ . Data related to density within  $0.45\text{--}0.65 \sigma^{-3}$  were used to calculate the contact angle.

Figure 4 presents the density and velocity profiles of gas-free water for nanochannels with rough walls cut into Si(100) and graphite under the external force field  $f_p = 0.05\sigma^3/\epsilon$ . Two characteristic boundary properties can be observed in Fig. 4. The first is substantially higher epitaxial layering distribution on the graphite substrate. The second is the similarity in boundary slip between the Si(100) and graphite walls. Layering occurred on most solid–fluid interfaces; however, the layering observed in the graphite samples was particularly distinct inside the groove and atop the ridge. The compact atomic arrangement of the tangential platform induces a higher probability of solid–fluid momentum exchange, resulting in higher epitaxial layering distribution. At the same time, the higher probability of solid–fluid momentum exchange also reduces slip length (Soong et al. 2007). A comparison of the parameters of wall–fluid interaction between silicon and graphite revealed that the wall–fluid interaction lengths were close; however, the graphite–water interaction energy

was far lower than that of the silicon–water interaction energy ( $\varepsilon_{C-O} < \varepsilon_{Si-O}$ , as shown in Table 1). This implies that the solid–fluid interaction length can be considered a fixed variable in this study. The lower graphite–water interaction energy reduced wall–fluid momentum exchange, thereby increasing the slip length. These two opposite effects resulted in close values for the slip length between the two rough walls in this study. It should be noted that a flat graphite substrate presents considerable hydrophilic-slip, due to the tight atomic arrangement on the tangential plane. Ho et al. (2011) indicated that the lattice of a hydrophilic surface could be arranged with a high density of adsorption sites, thereby allowing water molecules to migrate easily from one adsorption site to the next resulting in liquid slip. Similar conclusions were reached in simulations using the DPD method (Kasiteropoulou et al. 2011), in which slip length increased with surface density. However, this rapid migration is not observed on rough walls because the fluid molecules would be disturbed by the roughness features.

Thus, the above results are a good starting place to begin an investigation of the boundary conditions influenced by interfacial gas molecules coupling with various solid arrangements. Before investigating the properties observed at the argon–water interface, it is worth discussing the variation in density between the interface and the bulk region. Figure 5 illustrates a dramatic increase in the density of argon in the vicinity of the roughened substrate. The concentration of argon in the bulk fluid (water) was nearly independent of the density of argon at the interface. The concentration of argon in the bulk fluid (water) was approximately  $(2.25 \pm 1.75) \times 10^{-3} \sigma^{-3}$ . In the vicinity of the roughened substrate, the promotion of argon density is approximately 2–3 orders of magnitude over the argon density in the bulk fluid. The high interfacial gas density occurring on the Si(100) and graphite substrates can be attributed to the surface tension of surrounding water and the network of hydrogen bonds among water molecules, which is stronger than the argon–water interaction. Thus, the argon molecules are excluded from the bulk water, resulting in their accumulation on the substrate (Wang et al. 2008; Lee and Aluru 2011). According to the accumulation of gas molecules on the patterned surface, the interfacial density of argon molecules at the solid–fluid interface is defined as  $\rho_{s,Ar} \sigma^2 \equiv N_{Ar}/S$ , where  $N_{Ar}$  is the number of argon molecules near the substrate and  $S$  is the projected area of a given surface.

Three control parameters were tuned to alter the properties of interest. (I) To simulate the differences between the solid materials, the solid arrangement and solid–fluid interaction parameters were adjusted. (II) To identify the effects of argon concentration, the number of argon molecules was

changed from  $N_{Ar} = 0$  (pure water) to a finite value  $N_{Ar} = 351$  (corresponding to the number of water molecules  $N_{water} = 4,849 - 5,716$ ) in the initial setup stage. (III) To determine the shear rate effect, the external force fields were varied from  $f_p = 0.01 \sigma^3/\varepsilon$  to  $0.05 \sigma^3/\varepsilon$ .

### 3.1 Hydrodynamic effects

This section focuses on the morphology of nanoscale argon bubbles and the fluid density within the grooves under the influence of hydrodynamic effects. The external force fields included in the simulation cases in this section were fixed at  $f_p = 0.02 \sigma^3/\varepsilon$ . Argon and water density within the nanochannels of the (a) Si(100) and (b) graphite substrate are presented in Fig. 5. The left and middle plots in Fig. 5 illustrate the argon density contours before and after the addition of an external force field. The plot on the right presents liquid and argon density profiles (hydrostatic state on the left; Poiseuille flow on the right). Argon density at the interface  $\rho_{s,Ar} \sigma^2$  was approximately 0.4 for the cases in Fig. 5. Despite the potential for a monolayer of gas particles to be adsorbed on the solid–fluid interface (Dammer and Lohse 2006), in this study argon nanobubbles accumulated on the roughened surfaces.

For the hydrostatic equilibrium simulations on the Si(100) substrates in Fig. 5a, argon molecules accumulated at high densities inside and in the vicinity of the grooves. Argon layering was observed only inside the grooves. In the simulation of non-equilibrium Poiseuille flow, an obvious decrease in argon densities was observed. The inserts in Fig. 5a present the local water densities in the vicinity of the grooves. The insert of middle plot shows the local water density of Poiseuille flow, indicating that the grooves either filled with water or remained nearly void of water. The grooves filled by water molecules presented a more compact arrangement of perpendicular surfaces inside the groove (the plane perpendicular to the direction of flow), and a higher wall–fluid interaction energy  $\varepsilon_{Si-O}$  made the grooves in the Si(100) substrate more hydrophilic, thereby inducing an easy flow of water into grooves via an external force field. Conversely, following the expulsion from some of the cavities, argon molecules accumulated in other grooves, thereby forming argon bubbles that protruded into the region of flow. These argon bubbles protruding into the region of flow can be considered a meniscus with high protrusion angle. The left and middle plots in Fig. 5a illustrate distinct differences in the morphologies of argon bubbles on the roughened surface of the Si(100) substrate. These bubble distributions indicate the unstable properties of gas bubbles on Si(100) in a hydrodynamic state.

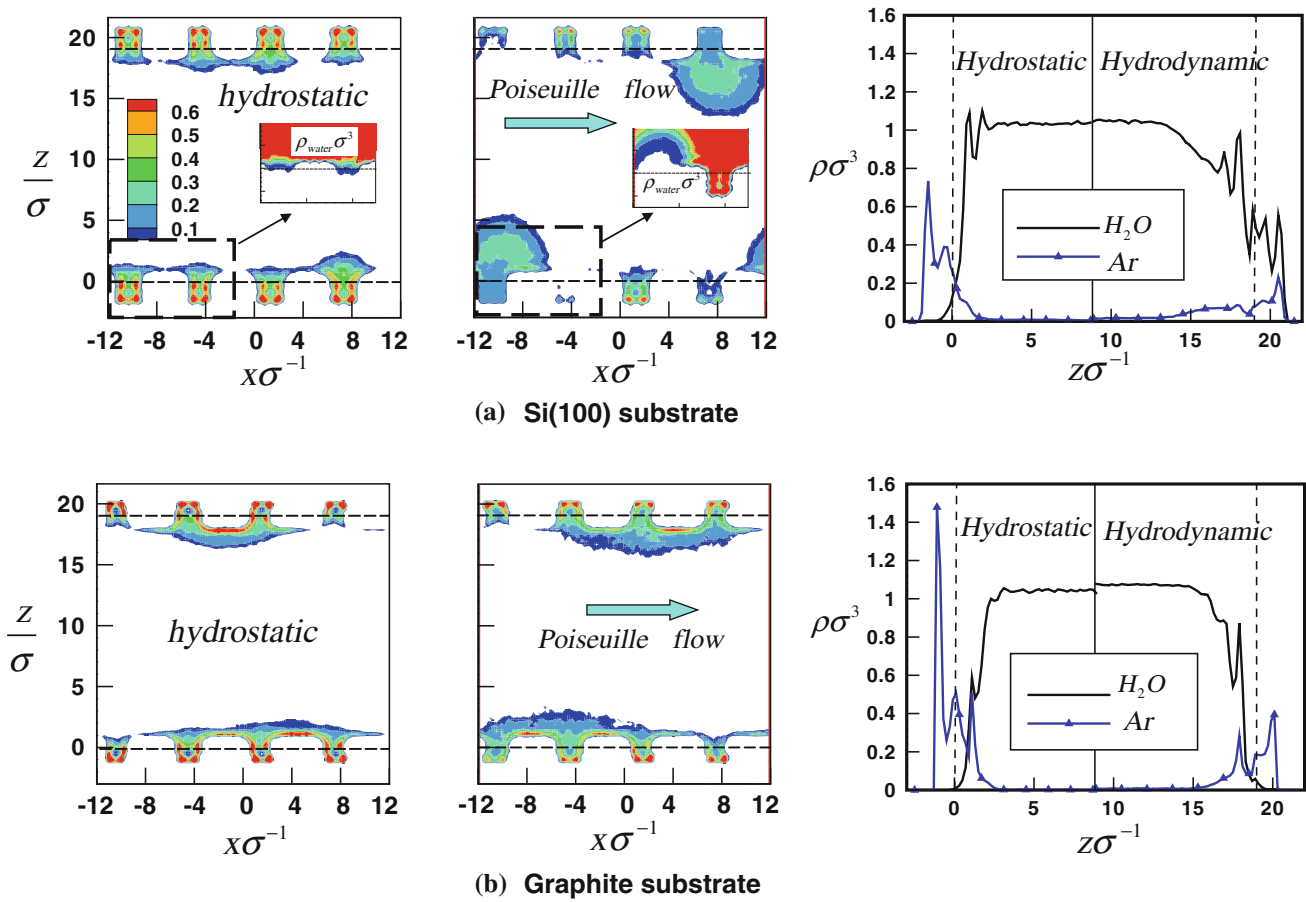


**Fig. 5** MD results of argon and water density within nanochannels of the (a) Si(100) and (b) graphite substrate. Argon density at the interface  $\rho_{S,Ar}\sigma^2$  was approximately 0.4 for the presented cases. The left and middle plots denote the argon density contours of hydrostatic and hydrodynamic states, respectively. The right plots present liquid

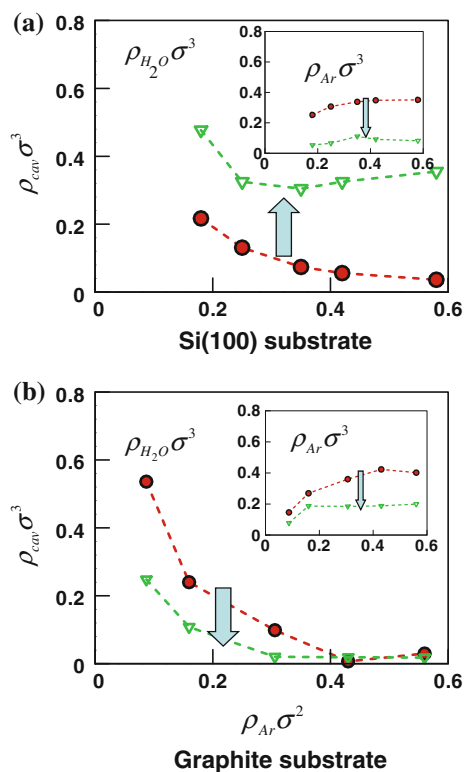
and argon density profiles (hydrostatic state on the left; Poiseuille flow on the right). The dashed lines denote the position of the first layer of solid atoms. The inset in a illustrate the local density of water molecules in the region of the grooves

Figure 5b presents the argon density contours and profiles on the roughened graphite substrate. Rather than a layering profile of high water density for the gas-free case on a graphite substrate, the magnitude of water density was reduced and argon density layering was promoted in the wall–fluid interfacial region, both in hydrostatic and hydrodynamic states. Compared with the results of the Si(100) substrate, the obvious layering of argon densities was observed both inside the groove and atop the solid ridge. The high argon density within the cavities, as shown in Fig. 5b, can be attributed to the high epitaxial layering of argon on the graphite substrate.

This high gas density is consistent with the findings of previous studies (Wang et al. 2008; Lee and Aluru 2011) which reported the accumulation of gas at water–graphite/water–graphene interfaces. High epitaxial layering of argon also flattened the argon bubble morphology, which made the bubbles more stable. Compared with the Si(100) substrate, the difference in bubble morphology between cases

with and without external force was only minor. High epitaxial layering of argon density on the tangential surface and the loose arrangement of grooves along the perpendicular plane made it difficult for water to enter the hydrophobic grooves in a hydrodynamic state. The amplitude of argon layering distribution was substantially reduced by hydrodynamic effects; however, a void remained within the groove before and after the addition of external pressure, as shown in the right plot of Fig. 5b. In addition, the protrusion angle of argon bubbles on the graphite substrates was less than that observed on the Si(100) surfaces. The relatively flattened meniscus of the bubble and the hydrophobic groove may have caused the water and solid surface to separate along a portion of the solid–fluid interface, thereby enhancing slip velocity.

Variations occurred in the morphology of interfacial argon bubbles on Si(100) and graphite substrates, despite similarities in the intrinsic contact angles of these two surfaces. According to our calculations, two factors can be



**Fig. 6** Averaged water density values inside the cavities versus interfacial argon density. The plots in **a** and **b** correspond to the results of the Si(100) and graphite substrates, respectively. The inserts are the results of averaged argon density values inside the cavities. The *arrows* inside the plots denote the direction of change from a hydrostatic to hydrodynamic state

attributed to the increase in the solid–fluid momentum exchange that promotes surface wettability: stronger solid–water interaction energy and higher surface density of the substrates. The Si(100) surface presented a higher solid–wall interaction energy while the graphite possesses a more compact atomic arrangement on the tangential plane. These two effects work together, resulting in similar contact angles and macroscopic indexes of Si(100) and graphite substrates. Conversely, these two effects exert a different influence on the morphology of the argon nanobubbles on roughened surfaces surrounded by aqueous solution. Compared with the argon–graphite interaction energy, a reduction in water–graphite interaction energy enhances the accumulation of gas molecules on the tangential plane (Dammer and Lohse 2006). In addition, the higher atomic surface density of graphite also increases the epitaxial layering of adjacent fluid. The gas enrichment and higher epitaxial layering both benefit the spreading of argon on the substrate, thereby inducing the argon molecules to fill the surface cavities and form argon bubbles with a flatter morphology. Conversely, due to the competition between water–silicon and argon–silicon interaction energy (the former is higher than the latter), most of the argon

molecules accumulated within the cavity regions and protruded into the region of flow.

The water density inside the grooves for hydrodynamic (empty symbols) and hydrostatic (filled symbols) versus interfacial argon density was compared using the same thermodynamic conditions in Fig. 6. The inserts of Fig. 6 present the average argon density versus interfacial argon density before and after the addition of pressure. In a hydrostatic state, an increase in argon concentration enhanced the argon density inside the grooves by as much as  $0.4 \sigma^{-3}$ , where it remained at a fixed value for both solid materials (shown as inserts). This implies that the argon accumulated beyond the baseline of the substrate to form the meniscus when the argon concentration exceeded the saturation value. Corresponding to the argon density, the water density  $\rho_{cav,H_2O} \sigma^3$  inside the grooves (indicated by filled symbols) decreased with an increase in argon density within the grooves. This also reveals that only a small number of water molecules remained inside the grooves when the argon density exceeded  $0.4$  ( $\rho_{cav,Ar} \sigma^3 > 0.4$ ).

The empty symbols in Fig. 6 represent the fluid density inside the grooves, in cases of Poiseuille flow simulation. The water density inside the grooves revealed that the external force field distinctly influences the solid materials, i.e., increases variation for the Si(100) surface and decreases variation for the graphite substrate. On the other hand, the argon densities inside the grooves presented a similar decrease in the variations between the two substrates with the addition of external pressure. The degree to which the range of argon density associated with a Si(100) substrate decreased inside the groove was much greater than that observed with the graphite substrate. On the rough Si(100) surface, the water molecules driven by pressure more easily enter the hydrophilic groove. However, the high water density inside the hydrophilic grooves also causes the argon bubbles to become increasingly unstable with regard to size, morphology, and position. On the graphite substrate, the argon density and layering magnitude inside the groove remained at a high level and hydrophobicity inside the grooves prevented an increase in water density. More stable and flattened bubbles are usually associated with gas accumulating on a hydrophobic substrate. It should be noted that only the perpendicular planes of grooves in a graphite substrate can be considered hydrophobic; therefore, the roughened graphite substrate is still considered a hydrophilic surface. This hydrophilic atomic arrangement along the tangential plane facilitated the spread of nanoscale argon bubbles on the substrate, which increased the slip velocity. The compact atomic arrangement along the tangential plane facilitated the spread of nanoscale argon bubbles on the substrate, which benefited the hydrophobicity of the cavities in the substrate.



### 3.2 Effects of gas concentration

In this section, we consider the effect of interfacial argon density on Poiseuille flow. An external force field was added to the simulation cases in this section, fixed at  $f_p = 0.02\sigma^3/\varepsilon$ . Figure 7 presents the velocity profiles and contours of water density and corresponding distributions of the average number of hydrogen bonds per water molecule  $\langle n_{HB} \rangle$  on a Si(100) surface. Figure 7a illustrates that the velocity distributions differ only slightly between the results of  $\rho_{S,Ar}\sigma^2 \sim 0.2$  and  $\sim 0.4$  except at the interface. This implies that the apparent slip length is influenced only slightly by gas bubbles when bubbles at the interface have a high protrusion angle and unstable properties. Figure 7b indicates the distribution of averaged  $\langle n_{HB} \rangle$  influenced by hydrodynamic effect and interfacial argon density. In a hydrostatic state, the averaged  $\langle n_{HB} \rangle$  maintains a value of approximately 3.45 except in the vicinity of the interface. However, these distributions decrease at the interface and increase in the region of flow when hydrodynamic effects are added. These changes in  $\langle n_{HB} \rangle$  may contribute to differences in the morphology of the argon bubbles.

To illustrate the influence of interfacial argon molecules on bubble morphology, we present the water density and averaged hydrogen bond contours of the corresponding cases in Fig. 7c and d, respectively. The contours show the close relationship between water density and  $\langle n_{HB} \rangle$ , according to variations in interfacial argon density.

Regions of high  $\langle n_{HB} \rangle$  inside the groove are locations in which water molecules could potentially be trapped. When the argon bubbles protrude into the region of flow, more argon molecules are involved; therefore, the  $\langle n_{HB} \rangle$  decreases in the corresponding region. On the margin of the argon bubbles, one can clearly observe a mixing layer, in which gas enrichment and reduced water density occur at the gas–liquid interface of the protruded bubble. This mixing layer benefits hydrogen bonding among the water molecules in the adjacent region due to the water molecule’s higher degree of freedom inside the mixing layer. A region with a  $\langle n_{HB} \rangle$  value beyond 3.5 does not present continuous distribution in the direction of flow. This periodic variation in  $\langle n_{HB} \rangle$  also indicates that the duration of hydrogen bonds would be reduced, thereby impeding the movement of fluids. This implies that the boundary velocity changed periodically, and the flow field was disturbed by the protrusion of bubbles and features on the substrate.

Figure 8 presents the results for the flow of water across the graphite substrate under similar conditions of roughness. The dependence of fluid velocity on interfacial argon density is presented in Fig. 8a. In this plot, slip velocity significantly increased with an increase in interfacial argon density. Similar to the results of Si(100), Fig. 8b shows the variation in  $\langle n_{HB} \rangle$  distribution induced by the hydrodynamic effect and interfacial argon density. Comparing with the results for Si(100) in a hydrodynamic state, the  $\langle n_{HB} \rangle$

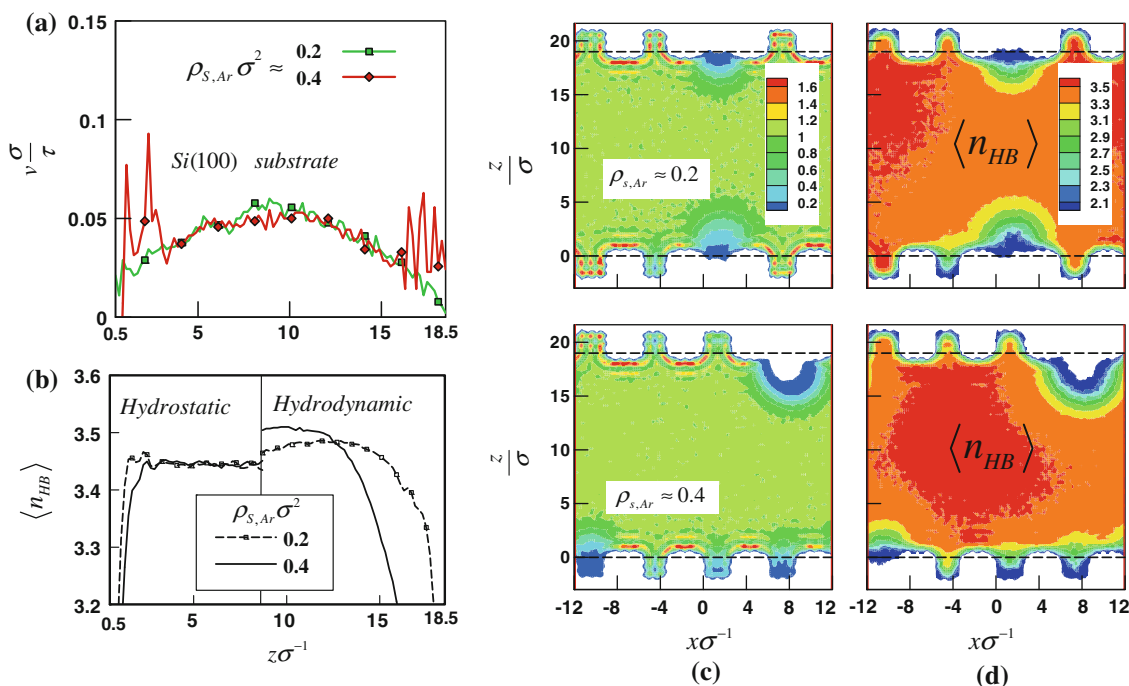


**Fig. 7** MD results of (a) velocity profiles (b) average number of hydrogen bonds per water molecule,  $n_{HB}$  profiles (hydrostatic state on the left; Poiseuille flow on the right) (c) water density and (d)  $n_{HB}$  contours on Si(100) with various argon densities at the interface

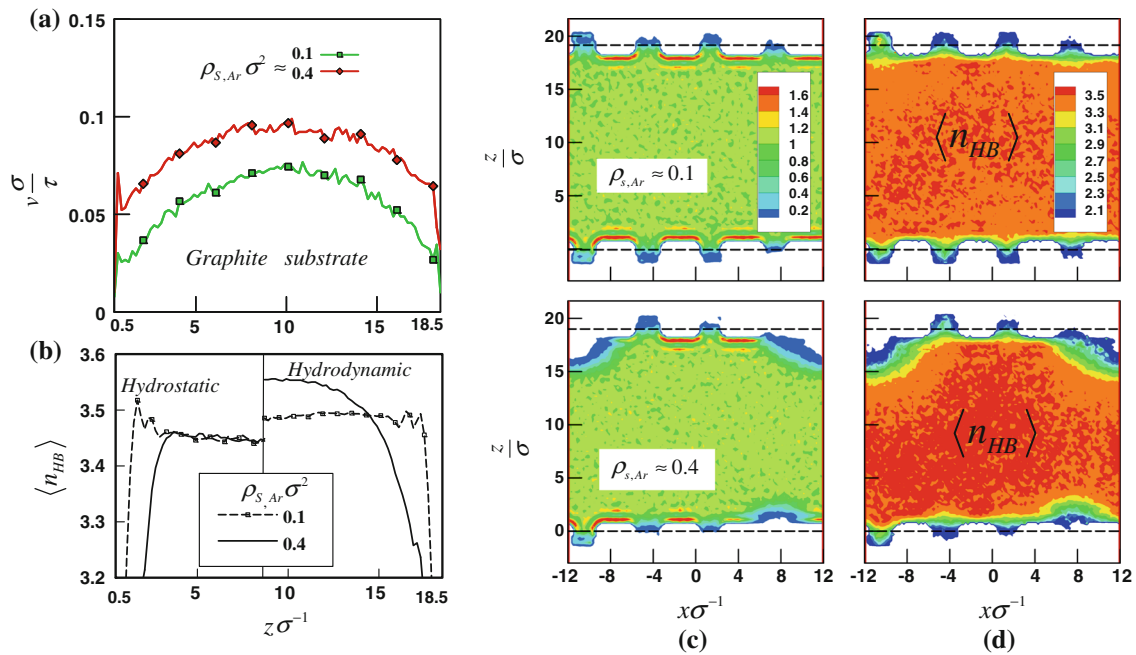


**Fig. 8** MD results of (a) velocity profiles (b) average number of hydrogen bond per water molecule,  $\langle n_{HB} \rangle$  profiles (hydrostatic state on the left; Poiseuille flow on the right) (c) water density and (d)  $\langle n_{HB} \rangle$  contours on graphite with various argon densities at the interface

distribution had an even stronger tendency to increase in the region of flow following an increase in interfacial argon density. The higher values for  $\langle n_{HB} \rangle$  in the central region of the channel also increased water density slightly beyond that observed in a hydrostatic state (shown in the right plot of Fig. 5b) due to the more compact accumulation of water molecules.

Figure 8c and d illustrates the water density and averaged  $\langle n_{HB} \rangle$  contours of  $\rho_{S,Ar}\sigma^2 \sim 0.1$  and 0.4. Compared with the Si(100) surface, far fewer water molecules remained inside the graphite grooves due to hydrophobicity inside the groove. In addition, the higher epitaxial layering of argon density also induced the flattening of bubbles beyond the baseline. Therefore, the high  $\langle n_{HB} \rangle$  in the central region of flow can be attributed to the more flattened bubble morphology and thus the distribution of the argon–water mixing layer as well. Moreover, the uniform  $n_{HB}$  distribution along the flow direction indicates the steady flow of water inside the nanochannel. The slip velocity promoted by an increase in interfacial argon density can be attributed to an increase in the area of low friction in the case of argon bubbles with a flattened meniscus. The flattened argon bubble resulted in a higher and more uniform  $\langle n_{HB} \rangle$  distribution in the central region of flow, which also contributes to maintaining the smooth flow of fluid. However, an increase in interfacial argon density caused the meniscus to assume a higher angle of protrusion, instead of spreading the gaseous film and thereby disturbing the flow field across both of the

substrates. Increasing the argon concentration does not promote the slip length when the gas density at the interface reaches a critical value. In addition, the interfacial argon density reaches a saturation value ( $\rho_{S,Ar}\sigma^2 \sim 0.6$  and  $\rho_{S,Ar}\sigma^2 \sim 0.7$  for Si(100) and graphite, respectively) with a further increase in the number of argon particles on the initial setting, because the liquid–gas–vapor coexistence procedure was adopted.

Figure 9 illustrates the effects of the interfacial density of argon molecules on apparent slip length. These results show that  $L_s$  on the graphite substrate increases greatly with an increase in interfacial argon density, while on the Si(100) substrate  $L_s$  was almost independent of  $\rho_{S,Ar}\sigma^2$ . This means that the interfacial gas enhanced the slip length only in the presence of obvious epitaxial gas layering when the groove in the substrate was hydrophobic. On rough graphite surfaces, high interfacial argon density with high epitaxial layering occupies most of the space in the grooves and flattens the meniscus beyond the baseline. Thus, the slip length increases with an increase in interfacial argon density as  $\rho_{S,Ar}\sigma^2$  remains in the range below 0.3. When the  $\rho_{S,Ar}\sigma^2$  increases beyond 0.3, the apparent slip length essentially becomes independent from interfacial argon density. With high  $\rho_{S,Ar}\sigma^2$  (and in turn large argon bubbles), nanochannel flow may encounter larger protruding bubbles and increased area of low friction. These two contradictory effects may be the reason that the slip length is almost independent of high interfacial argon density. On

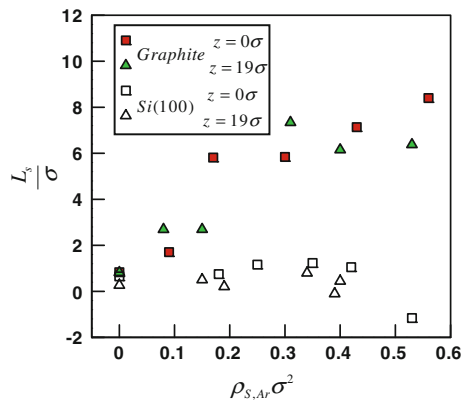


**Fig. 9** Slip length as a function of interfacial argon density. The *filled symbols* indicate results from graphite nanochannels, while the *empty symbols* were obtained from Si(100) nanochannels. The *square and triangle angle symbols* represent the values for slip length on the upper boundary and bottom boundary, respectively

the other hand, the grooves of Si(100) substrates either fill with argon bubbles which protrude into the region of flow or fill with water. The morphology of argon bubbles on Si(100) results in the slip length becoming negative when the interfacial argon density is sufficiently large.

### 3.3 Effects of shear rate

Because high slip length may be induced by gas at the solid/liquid interface, it is reasonable to expect that the apparent slip length should depend on the deformation of interfacial bubbles. Several studies have performed numerical investigations and simulations of interfacial gas-induced slip from a microscopic perspective. Hyväluoma and Harting (2008) and Hyväluoma et al. (2011) focused on shear flow over entrapped bubbles. The contact lines of these entrapped bubbles are pinned to the solid substrate. Their results indicated that bubble deformation due to shear rate can cause the slip length to decrease. Gao and Feng (2009) performed numerical simulations of shear flow over a periodically patterned substrate with entrapped gas bubbles. Their results revealed that the bubbles were transformed into a continuous gas film when the shear exceeded a critical value. These investigations represent important steps in this field; however, they are all based on specific assumptions, which ultimately led to different conclusions.

In this section, we investigated the effect of shear rate according to the results of a velocity profile and corresponding fluid morphology under external pressure of various degrees. The interfacial argon density in the cases in this section were fixed at approximately 0.4. Figure 10 shows the velocity profiles and the contours of water density on Si(100) substrates. As the shear rate increased, the bubbles were deformed resulting in fluctuations in the flow field. When the external force was increased, the

morphology of the argon bubble was deformed such that the local protrusion angle decreased on the upstream side of the bubble and increased on the downstream side. The contours of the deformed bubbles are presented in the bottom plot of Fig. 10b and the velocity profiles for two different external pressures are listed in Fig. 10a. Although, in our simulations, low slip velocity was observed in the cases involving a Si(100) substrate. The behavior of the bubbles included deformation and sliding.

Velocity profiles and a snapshot of water and argon molecules on graphite substrates are presented in Fig. 11. We adopted snapshot plots, rather than density contours, to illustrate the interfacial configuration because argon bubbles have high slip velocity across a graphite substrate. The morphology of the bubble in Fig. 11b revealed no significant deformation caused by shear rates associated with argon bubbles sliding along the surface.

Unlike the study of Gao and Feng (2009), in which the gasses transformed into a continuous gas film, the gas morphology maintained menisci on the solid substrate following an increase in external force. This could be attributed to the bubble sliding along the substrate and the high surface tension of surrounding water molecules. At the nanoscale, argon molecules are compressed to a high density, which tends to alter the behavior of the gas. Unlike the mechanical influence of flow through microchannels, the influence of shear force is much weaker than the capillary force upon a nanobubble’s morphology in cases with a roughened nanochannel. In the current study, enhanced slip velocity was observed with gas bubbles sliding on the roughened surface when the shear rate was increased. To examine the behavior of bubbles sliding across the substrate, we employed an index  $V_{Ar}\tau/\sigma$ , defined as argon bubble velocity along the wall–fluid interface, as shown in Fig. 12b. Most of the argon molecules near the substrate accumulated to form bubbles; therefore, it is reasonable to measure the velocity of these bubbles according to the average velocity of molecular argon within the near-wall region. In the current study, the velocity of interfacial argon bubbles was taken as the ensemble average of argon molecular velocity beyond the surface baseline and within the near-wall region of width  $2\sigma$  at a period  $300\tau$  to  $1,100\tau$ .

The velocity values for argon bubbles across the Si(100) substrate was nearly zero (in the range of  $\dot{\gamma}\tau \leq 0.015$ ), which then changed to a slight ascending trend with an increase in shear rate. In the graphite substrates, the argon bubbles slid along the direction of flow and the velocity increased with an increase in shear rate. However, as shown as Fig. 12a, the linear relationship between argon bubble velocity and shear rate caused the slip length to fluctuate slightly with an increase in shear rate. In this, our conclusions are consistent with those of LBM simulation

**Fig. 10** MD results of (a) velocity profiles and (b) water density contours on Si(100) substrate with various external force fields

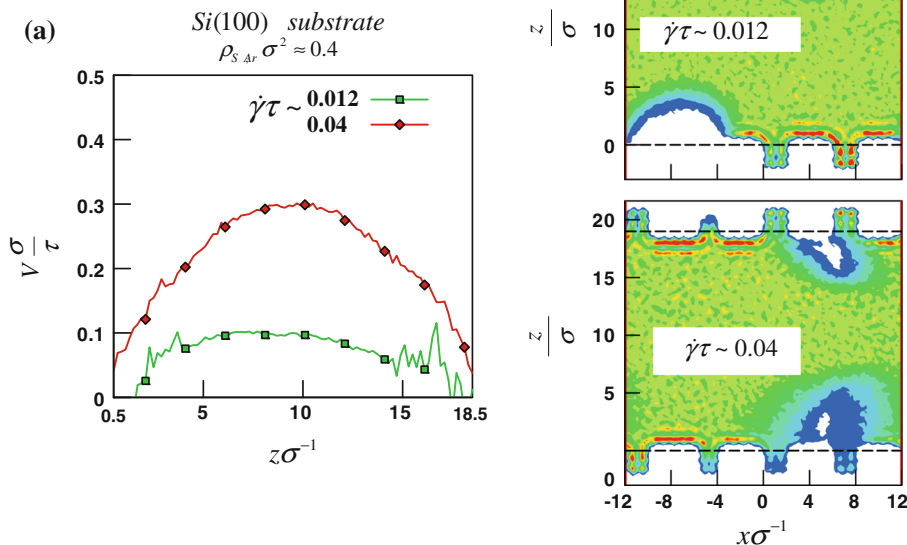
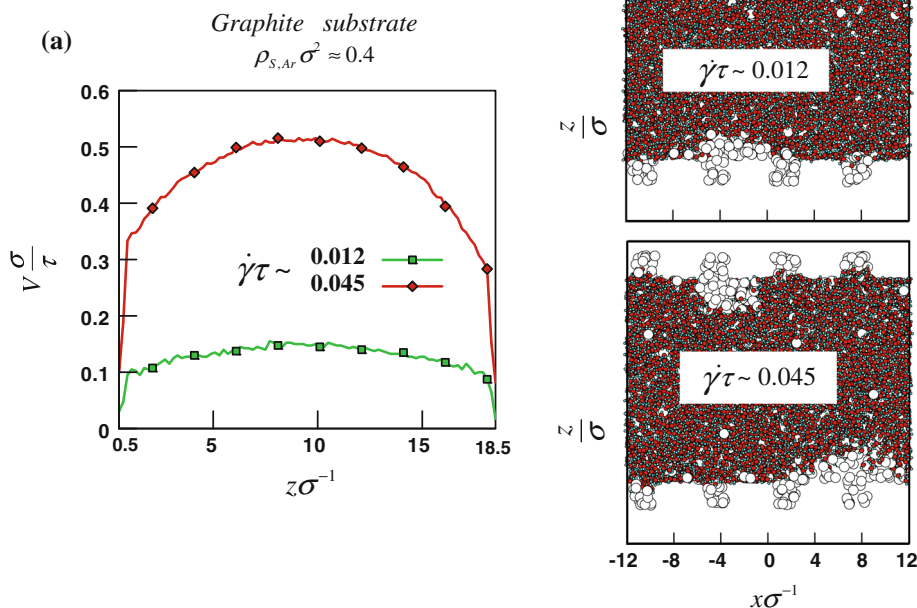


**Fig. 11** MD results of (a) velocity profiles and (b) fluid particle snapshot on graphite substrate with various external force fields



(Harting et al. 2010) and steady-state experiments (Cheng and Giordano 2002). These studies found that apparent slip length was nearly independent of shear rate. However, another dynamic experiment (Neto et al. 2003) reported that the slip length depends on shear rate. Some effects such as impurities or bubble growth induced by shear rate cannot be controlled by experiments. These effects may cause the conclusion of velocity dependence of the slip length (Harting et al. 2010).

Gao and Feng (2009) indicated that the contact lines of gas bubbles could be easily depinned to allow the bubbles to slide or even spread on a hydrophobic substrate. However, the roughened graphite substrate adopted in the current study was hydrophilic. In the case of gas-free fluid flow, roughness features may induce the hopping of fluid particles near the boundary and reduce apparent slip. Conversely, the existence of entrapped nanobubbles on a graphite substrate can cause the accumulation of gas in the



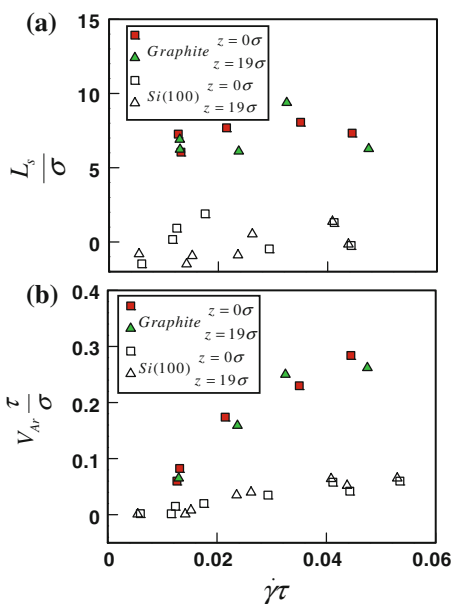


**Fig. 12** **a** Slip length and **b** velocity of interfacial argon bubbles as a function of shear rate. The *filled symbols* indicate results from graphite nanochannels, while the *empty symbols* were obtained from Si(100) nanochannels

grooved space such that the bubbles slide easily along the direction of flow. Because the velocity at which the bubbles slide is proportional to the fluid slip velocity on the baseline of the substrate, the slip of water with entrapped nanobubbles flowing over a rough graphite substrate can be attributed to the following aspects: the high slip velocity of argon bubbles on the substrate; the menisci of the bubbles protruding into the region of flow; and the filling of the grooved space by argon molecules, which prevent the hopping movement of water particles near the substrate. These mechanisms of boundary slip differ somewhat from the large slip associated with super-hydrophobic surfaces in which the liquid rests on rough features due to surface tension and gas particles can be found along most of the liquid boundary.

**4 Concluding remarks**

This MD study adopted two hydrophilic rough wall nanochannels with hydrophilic and hydrophobic grooves, i.e., Si(100) and graphite, respectively. The aim was to investigate the effects of solids on the interfacial properties of flowing water containing gas. For both contact angle and slip length, the gas-free water possessed similar values for both of the substrates, despite differences in atomic arrangement and solid–fluid interfacial parameters. Using this as a starting point, we simulated various concentrations of argon and shear rates to investigate the interfacial

properties within the roughened nanochannels. However, it should be noted that a number of other important effects associated with roughness geometry have not been discussed in the present study. Further work remains to be done to elucidate the effects of surface fraction, pattern period, amplitude, and roughness shape.

Despite the fact that the presence of interfacial gas molecules alters the contact angle, the present results show no obvious relationship between the slip length and contact angle of the substrate. This result is similar to the conclusions presented by Gu and Chen (2011), in which the slip length decreases with an increase in the effects of interfacial curvature in the direction of flow. Conversely, a quasi-universal function proposed by Huang et al. (2008) with the form  $L_s \propto (\cos \theta + 1)^{-2}$  is based on the following relationships: between slip length and  $\epsilon_{wf}$  (i.e.,  $L_s \propto \epsilon_{wf}^{-2}$ ) and between contact angle and  $\epsilon_{wf}$  (i.e.,  $\cos \theta + 1 \propto \epsilon_{wf}$ ), where  $\epsilon_{wf}$  is the wall–fluid interaction energy. The  $\theta - L_s$  equation implies that wall–fluid interaction energy can be adopted as a characteristic property of wall–fluid interface in both static and dynamic fluid fields. However, the interfacial properties observed in the present study included solid–wall interactions as well as surface roughness, bubble morphology, solid–gas, and gas–fluid interaction. From the viewpoint of molecular interaction, the  $\theta - L_s$  equation does not necessarily provide an adequate solution to the problem of gas-containing fluid in rough wall nanochannels.

Based on the MD simulations, the physical findings can be summarized as follows:

1. The slip lengths of water flow on Si(100) and graphite substrates present distinct differences under the effects of interfacial gas concentration. In cases of low shear rate (low velocity gas bubbles), the slip length is determined by two competing effects (1) increased boundary roughness induced by the protrusion of bubbles and nanogrooves within the substrate; and (2) increased area of low friction at gas–liquid interface (in the case of flat bubbles). The boundary slip on the graphite substrate was enhanced by the increase in argon concentration when  $\rho_{S,Ar}\sigma^2$  was below 0.3. With high  $\rho_{S,Ar}\sigma^2$  and in turn, large argon bubbles, flow through the nanochannels may result in an increase in the area of low friction and encountering larger protruding bubbles. Further increasing the interfacial argon density resulted in the apparent slip length approaching a constant value. On the other hand, the grooves of Si(100) substrates either filled with argon bubbles, which protruded into the region of flow or filled with water, thereby causing sticky conditions at the boundary between the surface Si(100), due to an

increase in interfacial gas. These results show that interfacial gas enhanced the slip length only when the phenomenon of epitaxial gas layering was observed and the groove of the substrate was hydrophobic. This implies that the wall–fluid parameters at the microscopic level and the wettability inside cavities on the substrate should be considered when determining the slip length associated with the passage of water through roughened hydrophilic walls with entrapped nanobubbles of gas.

2. The results of water density within the grooves demonstrated that the influences of hydrodynamics are quite distinct for solid materials. In this study, this meant an increase in variation for Si(100) surfaces and a decrease in variation for the graphite substrate. On the other hand, the density of argon inside the grooves had a similar decreasing effect on the two substrates following an increase in external pressure. Distinctly different morphologies were observed in the argon bubbles on roughened Si(100) surfaces before and after the addition of an external force field. The difference in bubble morphology between cases with and without external force was far less pronounced with the graphite samples. On the roughened Si(100) surface, the water molecules driven by pressure entered the hydrophilic groove more easily. These hydrophilic grooves also increased the instability of the entrapped argon bubbles with regard to size, morphology, and position. On a graphite substrate, the argon density and layering magnitude inside the grooves remained high and the hydrophobicity of the grooves prevented an increase in water density inside the grooves. The tangential compact atomic arrangement of the graphite facilitated the spread of nanoscale argon bubbles across the substrate and a normal loose arrangement benefited the hydrophobicity of cavities within the substrate.
3. This study demonstrated that rather than transforming into a continuous gas film, as occurred in the research of Gao and Feng (2009), the gas morphology maintained its menisci on the solid substrate following an increase in external force. In addition, rather than pinned on the substrate, as in the research of Hyväluoma and Harting (2008), an increase in slip velocity was observed with gas bubbles sliding on the roughened surface when the shear rate was increased. The behavior of the entrapped nanobubbles, including deformation and sliding, was observed when external pressure was added. Bubble deformation was observed for fluid passing a roughened Si(100) substrate with low slip velocity. On the other hand, only slight bubble deformation occurred with high sliding velocity passing the roughened graphite substrates. Bubble slid

velocity increased with an increase in shear rate on both rough Si(100) and graphite substrates. This effect was far more pronounced on rough graphite walls than on rough Si(100) substrates. The present results demonstrate that the linear relationship between argon bubble velocity and shear rate caused the apparent slip length almost independent of shear rate.

**Acknowledgments** This study was supported by the National Science Council of the R. O. C. (Taiwan) through the Grant NSC 101-2221-E-012-002-MY2.

## References

- Argyris D, Tummala NR, Striolo A, Cole DR (2008) Molecular structure and dynamics in thin water films at the silica and graphite surfaces. *J Phys Chem C* 112(35):13587–13599
- Bocquet L, Barrat JL (2007) Flow boundary conditions from nano- to micro-scales. *Soft Matter* 3(6):685–693
- Bonaccorso E, Butt HJ, Craig VS (2003) Surface roughness and hydrodynamic boundary slip of a Newtonian fluid in a completely wetting system. *Phys Rev Lett* 90:144501
- Cao BY, Chen M, Guo ZY (2006) Liquid flow in surface-nanostructured channels studied by molecular dynamics simulation. *Phys Rev E* 74:066311
- Cao BY, Sun J, Chen M, Guo ZY (2009) Molecular momentum transport at fluid–solid interfaces in MEMS/NEMS: a review. *Int J Mol Sci* 10(11):4638–4706
- Cheng JT, Giordano N (2002) Fluid flow through nanometer-scale channels. *Phys Rev E* 65:031206
- Cottin-Bizonne C, Barrat JL, Bocquet L, Charlaix E (2003) Low-friction flows of liquid at nanopatterned interfaces. *Nat Mater* 2(4):237–240
- Dammer SM, Lohse D (2006) Gas enrichment at liquid–wall interfaces. *Phys Rev Lett* 96:206101
- Gao P, Feng JJ (2009) Enhanced slip on a patterned substrate due to depinning of contact line. *Phys Fluids* 21:102102
- Gordillo MC, Martí J (2010) Effect of surface roughness on the static and dynamic properties of water adsorbed on graphene. *J Phys Chem B* 114(13):4583–4589
- Gu X, Chen M (2011) Shape dependence of slip length on patterned hydrophobic surfaces. *Appl Phys Lett* 99(6):063101
- Harting J, Kunert C, Hyväluoma J (2010) Lattice Boltzmann simulations in microfluidics: probing the no-slip boundary condition in hydrophobic, rough, and surface nanobubble laden microchannels. *Microfluid Nanofluid* 8(1):1–10
- Ho TA, Papavassiliou DV, Lee LL, Striolo A (2011) Liquid water can slip on a hydrophilic surface. *Proc Natl Acad Sci* 108(39):16170–16175
- Huang DM, Sender C, Horinek D, Netz RR, Bocquet L (2008) Water slippage versus contact angle: a quasiuniversal relationship. *Phys Rev Lett* 101:226101
- Hyväluoma J, Harting J (2008) Slip flow over structured surfaces with entrapped microbubbles. *Phys Rev Lett* 100:246001
- Hyväluoma J, Kunert C, Harting J (2011) Simulations of slip flow on nanobubble-laden surfaces. *J Phys Cond Matter* 23(18):184106
- Joly L, Ybert C, Trizac E, Bocquet L (2004) Hydrodynamics within the electric double layer on slipping surfaces. *Phys Rev Lett* 93:257805
- Joseph S, Aluru NR (2008) Why are carbon nanotubes fast transporters of water? *Nano Lett* 8(2):452–458

- Kasiteropoulou D, Karakasidis TE, Liakopoulos A (2011) Dissipative particle dynamics investigation of parameters affecting planar nanochannel flows. *Mater Sci Eng, B* 176(19):1574–1579
- Kasiteropoulou D, Karakasidis TE, Liakopoulos A (2012) A dissipative particle dynamics study of flow in periodically grooved nanochannels. *Int J Numer Methods Fluids* 68(9):1156–1172
- Kim D, Darve E (2006) Molecular dynamics simulation of electro-osmotic flows in rough wall nanochannels. *Phys Rev E* 73:051203
- Lauga E, Brenner MP, Stone HA (2005) Microfluidics: the no-slip boundary condition. In: Foss J et al (eds) *Experimental fluid dynamics*, Ch15. Springer, New York
- Lee J, Aluru NR (2011) Mechanistic analysis of gas enrichment in gas–water mixtures near extended surfaces. *J Phys Chem C* 115(35):17495–17502
- Maali A, Cohen-Bouhacina T, Kellay H (2008) Measurement of the slip length of water flow on graphite surface. *Appl Phys Lett* 92(5):053101
- Martí J (1999) Analysis of the hydrogen bonding and vibrational spectra of supercritical model water by molecular dynamics simulations. *J Chem Phys* 110:6876
- Martini A, Hsu HY, Patankar NA, Lichter S (2008) Slip at high shear rates. *Phys Rev Lett* 100(20):206001
- Neto C, Craig VSJ, Williams DRM (2003) Evidence of shear-dependent boundary slip in Newtonian liquids. *Eur Phys J E* 12(1):71–74
- Priezjev NV, Darhuber AA, Troian SM (2005) Slip behavior in liquid films on surfaces of patterned wettability: comparison between continuum and molecular dynamics simulations. *Phys Rev E* 71(4):041608
- Quééré D (2008) Wetting and roughness. *Annu Rev Mater Res* 38:71–99
- Rapaport DC (2004) *The art of molecular dynamics simulation*. Cambridge university press, Cambridge
- Sbragaglia M, Benzi R, Biferale L, Succi S, Toschi F (2006) Surface roughness-hydrophobicity coupling in microchannel and nanochannel flows. *Phys Rev Lett* 97(20):204503
- Sendner C, Horinek D, Bocquet L, Netz RR (2009) Interfacial water at hydrophobic and hydrophilic surfaces: slip, viscosity, and diffusion. *Langmuir* 25(18):10768–10781
- Sofos F, Karakasidis TE, Liakopoulos A (2009) Transport properties of liquid argon in krypton nanochannels: anisotropy and non-homogeneity introduced by the solid walls. *Int J Heat Mass Transf* 52(3):735–743
- Sofos F, Karakasidis TE, Liakopoulos A (2012) Surface wettability effects on flow in rough wall nanochannels. *Microfluid Nano-fluid* 12:25–31
- Sofos F, Karakasidis TE, Liakopoulos A (2013) Parameters affecting slip length at the nanoscale. *J Comput Theor Nanosci* 10(3):648–650
- Soong CY, Yen TH, Tzeng PY (2007) Molecular dynamics simulation of nanochannel flows with effects of wall lattice-fluid interactions. *Phys Rev E* 76(3):036303
- Tandon V, Kirby BJ (2008) Zeta potential and electroosmotic mobility in microfluidic devices fabricated from hydrophobic polymers: 2 slip and interfacial water structure. *Electrophoresis* 29(5):1102–1114
- Thompson PA, Troian SM (1997) A general boundary condition for liquid flow at solid surfaces. *Nature* 389:360–362
- Tretheway DC, Meinhart CD (2004) A generating mechanism for apparent fluid slip in hydrophobic microchannels. *Phys Fluids* 16:1509
- Tretyakov N, Müller M (2013) Correlation between surface topography and slippage: a molecular dynamics study. *Soft Matter* 9:3613–3623
- Vinogradova OI, Belyaev AV (2011) Wetting, roughness and flow boundary conditions. *J Phys Cond Matter* 23(18):184104
- Wang CL, Li ZX, Li JY, Xiu P, Hu J, Fang HP (2008) High density gas state at water/graphite interface studied by molecular dynamics simulation. *Chin Phys B* 17(7):2646
- Yen TH (2011) Wetting characteristics of nanoscale water droplet on silicon substrates with effects of surface morphology. *Mol Simul* 37(9):766–778
- Zhu Y, Granick S (2001) Rate-dependent slip of Newtonian liquid at smooth surfaces. *Phys Rev Lett* 87(9):096105
- Zhu Y, Granick S (2002) Limits of the hydrodynamic no-slip boundary condition. *Phys Rev Lett* 88(10):106102
- Zhu W, Singer SJ, Zheng Z, Conlisk AT (2005) Electro-osmotic flow of a model electrolyte. *Phys Rev E* 71(4):041501